Check for updates

AGU ADVANCING EARTH AND SPACE SCIENCES

Geophysical Research Letters®

RESEARCH LETTER
10.1029/2025GL115545

Do Observations Support Ideas Behind Common Mass Flux Closures?

R. Vogel[1] and J. P. Mellado[1]

[1]Meteorological Institute, Universität Hamburg, Hamburg, Germany

Abstract The cloud-base mass flux closure is a critical component of convective parameterizations and usually consists of scalings for the cloud(-core) area fraction and vertical velocity. Here we evaluate if observations from the EUREC^{4}A campaign support ideas behind two common closures. All closure parameters are diagnosed at the mesoscale from dropsonde data and turbulence measurements. The closure models are compared to the observed mass flux estimated as a residual of the sub-cloud layer mass budget from the same dropsonde arrays. Both closures capture the magnitude of the reference mass flux. However, the closure based on the surface-based convective velocity scale strongly underestimates mass flux variability, whereas the closure using a convective inhibition based area fraction and turbulence kinetic energy (TKE) based vertical velocity scale strongly overestimates it. TKE alone explains nearly 80% of mass flux variability, suggesting that TKE aggregates information of area fraction and vertical velocity of cloud-base updrafts.

Plain Language Summary Due to their small size compared to the size of typical weather and climate model gridboxes, shallow cumulus clouds and the vertical transport of moisture, heat, and momentum they accomplish have to be represented with sets of simplified equations. One such “closure” equation is used to compute the mass flux at cloud base, which determines the overall intensity of convection in a gridbox. In the recent EUREC^{4}A field campaign, we collected for the first time the necessary observations to estimate this cloud-base mass flux on the scale of a typical climate model gridbox. Here we use these observations to test the physical ideas behind two common closure equations. We find these closures to represent the mean observed mass flux very well. The variability of the mass flux, however, is strongly underestimated in one closure and overestimated in the other. The data demonstrates that more than 80% of the mass flux variability can be explained by the kinetic energy of sub-cloud layer eddies, which build the roots of the shallow cumuli. Our study highlights a path to better represent convective mass fluxes in weather and climate models, which is essential for accurate simulations of shallow cumuli and their climate feedback.

Key Points:

- The accuracy and scale of EUREC^{4}A observations allows testing of physical ideas in mass flux closures
- The evaluated closures capture the magnitude and explain about 20% of the observed mass flux variability
- Turbulence kinetic energy alone explains 80% of mass flux variability, highlighting the tight coupling of clouds to the sub-cloud layer

Correspondence to:

R. Vogel,
raphaela.vogel@uni-hamburg.de

Citation:

Vogel, R., & Mellado, J. P. (2025). Do observations support ideas behind common mass flux closures? *Geophysical Research Letters*, *52*, e2025GL115545. https://doi.org/10.1029/2025GL115545

Received 24 FEB 2025
Accepted 18 JUL 2025

Author Contributions:

Conceptualization: R. Vogel, J. P. Mellado
Data curation: R. Vogel
Formal analysis: R. Vogel
Funding acquisition: R. Vogel, J. P. Mellado
Investigation: R. Vogel
Methodology: R. Vogel, J. P. Mellado
Project administration: R. Vogel
Resources: R. Vogel
Software: R. Vogel
Validation: R. Vogel
Visualization: R. Vogel
Writing – original draft: R. Vogel
Writing – review & editing: R. Vogel, J. P. Mellado

1. Introduction

Observations from the EUREC^{4}A field campaign (Bony et al., 2017; Stevens et al., 2021) demonstrate the critical role of the cloud-base mass flux in controlling trade cumulus cloudiness. The EUREC^{4}A data shows that a stronger convective mass flux (and thus stronger convective mixing) is associated with a larger cloud fraction near the base of the cumulus layer (Vogel et al., 2022). This observational finding refutes the *mixing-desiccation hypothesis*, a key hypothesis for a large positive trade cumulus feedback operating in models with a high climate sensitivity (Sherwood et al., 2014; Vial et al., 2016). The mixing-desiccation mechanism contends that an increasing mass flux leads to a deepening of clouds, which is compensated by enhanced downward transport of dry air from higher levels, leading to a drying of the lower cloud layer and a reduction of cloudiness at the base of the cumulus layer. Whether cloud deepening leads to sub-cloud layer drying has been studied with large-scale budgets and aircraft data since the large field campaigns in the 1970s (e.g., Augstein et al., 1973; Esbensen, 1975; Nicholls & LeMone, 1980), showing the desiccation to be a function of scale. EUREC^{4}A targeted the 200 km mesoscale, which is a typical grid spacing of coarse climate models and allows to compare the observed relationships with the models. The current generation of climate models only poorly represents the magnitude and variability of the observed cloud-base mass flux and cloudiness, and strongly underestimates their tight positive correlation (Vial et al., 2023; Vogel et al., 2022). Here we focus on one specific factor that could contribute to these model-observation discrepancies—the cloud-base mass flux—and test if the physical assumptions underlying common mass flux closures are consistent with the EUREC^{4}A observations.

The closure for the cloud-base mass flux, M, is a key component of convective parameterizations and determines the overall intensity of convection in a grid box (Siebesma et al., 2020). M is usually defined as the product of a mean cloud(–core) area fraction, a_c, and a mean cloud(–core) vertical velocity, w_c,

$$M = a_\mathrm{c} w_\mathrm{c}. \tag{1}$$

Note that we neglect multiplication by the air density here, as the density is usually assumed constant (Lamer et al., 2015; Vogel et al., 2022). Our mass fluxes are thus (mass) specific mass fluxes with units of velocity (L T^{-1}).

The task of a closure is to come up with scalings representing the two terms in Equation 1. Closure methods are typically developed and tested based on large-eddy simulations of a small number of idealized cases with limited variability in equilibrium cloud-base mass fluxes (Fletcher & Bretherton, 2010; Grant, 2001; Neggers et al., 2009). The simulated mass fluxes used to fit the closure model of Grant (2001) for example, span a range from only 19–24 mm s^{-1}, which is just a fifth of the observed variability in typical winter trade conditions during EUREC^{4}A (Vogel et al., 2022). It is thus unclear how well the closures represent the mass flux in more variable conditions.

Why should one still care about cloud-base mass flux closures when global models are run at increasingly high resolution that allows them to switch-off convective parameterizations (Stevens et al., 2019)? First, confronting the closure assumptions with observations can improve our fundamental understanding of the convective and turbulent processes involved. And second, even deep convection is not fully resolved at kilometer-scale grid spacings and an improved mass flux closure accounting for moisture advection was shown to improve the representation of organized systems and their rain properties in kilometer-scale simulations (Becker et al., 2021). Especially for operational models, convective parameterizations will therefore continue to be essential. Shallow convection only starts to be resolved at hectometer-scale grid spacings, so evaluating shallow-convective mass flux closures remains particularly pertinent.

In the following, we first explain the ideas behind the evaluated mass flux closures (Section 2). Section 3 describes how the EUREC^{4}A observations are used to estimate the reference mass flux and diagnose the closure parameters. The results are discussed in Section 4, and the conclusions presented in Section 5.

2. Evaluated Mass Flux Closures

Due to the large impact and uncertainty associated with the unresolved turbulent and convective processes on the simulated weather and climate, the improvement of paramaterizations has long been an active area of research. A critical challenge has been the unification of previously separate parameterizations of boundary layer turbulence, dry, and shallow convection. A popular and successful approach to do so is the eddy-diffusivity mass-flux (EDMF) framework that combines a mass-flux formulation representing the non-local transport by organized thermal updrafts with an eddy-diffusivity model representing the local turbulent mixing in the non-convective environment (Siebesma et al., 2007; Soares et al., 2004). The flexibility of the EDMF framework motivated continued developments including the use of stochastic models, multiplume models, consistent coupling to microphysics, or the use of higher-order closures using assumed probability density functions (e.g., Neggers, 2015; Suselj et al., 2019; Witte et al., 2022). While all these aspects are relevant for a realistic simulation of turbulent and convective processes, at the heart of the problem lie the two main properties a_c and w_c. In this study we therefore focus on simple scalings for these two.

We evaluate two common closures, the closure of Grant (2001) using the surface-based convective velocity scale (w_*) and the closure of Park and Bretherton (2009) using a convective inhibition (CIN) based area fraction and a turbulence kinetic energy (TKE) based vertical velocity scale (hereafter the closures are referred to as G01 and PB09, respectively). This choice is motivated by the fact that (a) the two closures differ in fundamental assumptions about the physical phenomena behind the scalings of w_c and a_c that are testable with measurements, (b) the parameters of the closures can be diagnosed directly from the available EUREC^{4}A observations without any major assumptions, and (c) the closures were specifically designed for shallow convection, in contrast to e.g. the deep convection closures based on convective available potential energy adjustment (e.g., Arakawa &

Schubert, 1974). In the following, the conceptual ideas behind the closures are briefly introduced. A more detailed description can be found in the original publications.

The simple closure of G01 relates M to the sub-cloud layer TKE, noting that active cumuli are rooted deeply in the sub-cloud layer (LeMone & Pennell, 1976) and thus can be linked to the kinetic energy of sub-cloud updrafts. Based on a simplified TKE budget equation and under the assumption that the main source of TKE is convection driven by the surface buoyancy flux, G01 scaled M with the surface-based convective velocity scale w_* (Deardorff, 1970). w_* is defined as $w_* = \left(h \frac{g}{\theta_{v,s}} \overline{w'\theta_v'}\big|_s\right)^{1/3}$, where g is the gravitational acceleration, $\theta_{v,s}$ is the virtual potential temperature near the surface, h the sub-cloud layer depth, and $\overline{w'\theta_v'}\big|_s$ is the surface buoyancy flux. A linear regression between the conditionally sampled cloud-core mass flux and w_* of five idealized large-eddy simulations then led to the following closure equation:

$$M_{G01} = 0.03 w_*. \quad (2)$$

The G01 closure is used in both climate models (e.g., Walters et al., 2017; von Salzen et al., 2013) and operational weather models (e.g., de Rooy et al., 2022).

The second closure evaluated is the closure based on boundary layer CIN implemented in the University of Washington shallow convection scheme (Bretherton et al., 2004), as modified by PB09. To model the cloud vertical velocity scale, the closure uses the resolved TKE averaged over the layer below cloud base (Fletcher & Bretherton, 2010) and thus also includes contributions from shear-driven turbulence (instead of only the convective contribution represented by w_*). The PB09 closure explicitly represents an area fraction scale depending on the ratio of CIN and TKE, which relates the updraft kinetic energy to the potential energy barrier the updrafts have to overcome at the sub-cloud layer top. The resulting closure equation is:

$$M_{PB09} = 0.4\sqrt{\mathrm{TKE}}\,\exp(-\mathrm{CIN}/\mathrm{TKE}). \quad (3)$$

The original formulation also includes multiplication by the air density, which we ignore here. For the PB09 closure to be used in a convection scheme, the TKE must be provided by the boundary layer or turbulence schemes. The closure is for example, used in the MIROC6 climate model (Tatebe et al., 2019).

3. Observations

3.1. EUREC^{4}A Field Campaign Data

EUREC^{4}A stands for *Elucidating the role of cloud-circulation coupling in climate* and was a large international field campaign that took place in January-February 2020 (Bony et al., 2017; Stevens et al., 2021). EUREC^{4}A sampled typical trade-wind conditions agreeing with average Jan-Feb conditions in the region (Stevens et al., 2021; Vogel et al., 2022), with shallow trade cumulus clouds that regularly featured stratiform inversion cloud. Cloud cover and cloud top heights as sampled by the WALES lidar onboard the HALO aircraft (Konow et al., 2021) were $34.0 \pm 12.9\%$ and $1{,}600 \pm 390$ m (mean ± sd), respectively. Cold pools indicating deeper precipitating trade cumuli were present about 7% of the time (Touzé-Peiffer et al., 2022), consistent with a 10-year cold-pool climatology in the trades (Vogel et al., 2021).

We use the measurements of the HALO (Konow et al., 2021) and ATR (Bony et al., 2022) aircraft, which flew repeated 3 hr patterns in the 220 km-diameter "EUREC^{4}A circle" centered at 13.3°N, 57.7°W upstream Barbados (Figure 1). Per flight, the HALO aircraft flew two sets of three circles at 10.2 km altitude and released 12 dropsondes per circle, which measured the vertical profiles of thermodynamic and dynamic properties (George et al., 2021). Note that we omit all soundings that fell into cold pools following the criteria of a shallow mixed-layer from Touzé-Peiffer et al. (2022), as in Vogel et al. (2022). Simultaneously, the ATR aircraft flew two separate flights during the HALO circling period, each consisting of 2–3 rectangle-patterns in the EUREC^{4}A circle at the cloud-base level (i.e., the level of estimated maximum cloud-base cloud fraction), followed by two L-shaped *L-legs* near the top and the middle of the sub-cloud-layer (in along-wind and across-wind directions, between 200 and 600 m depending on conditions). The ATR aircraft collected extensive turbulence measurements with high-frequency (25 Hz) wind, temperature, and humidity sensors (Brilouet et al., 2021). To compute

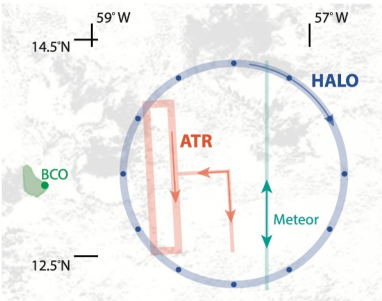

Figure 1. Overview of the area sampled by the HALO and ATR aircraft. Also shown are the transect of R/V *Meteor* and the location of the Barbados Cloud Observatory. The dots along the EUREC^{4}A circle flown by HALO represent the locations of dropsonde launches. See Stevens et al. (2021) for details.

the surface fluxes, we also use sea-surface temperatures (SSTs) measured by the R/V *Meteor* along its transect on the eastern side of the EUREC^{4}A circle.

Overall, the data set contains 24 sets of three circles, collected during 12 HALO flights. For 13 of the 3-circle sets, coincident ATR turbulence data are available.

3.2. Reference Mass Flux Observations

To evaluate the mass flux determined by the two closures for the EUREC^{4}A data, we compare their magnitude and variability with the observed mass flux M_{OBS} estimated as a residual of the sub-cloud layer mass budget, as derived in Vogel et al. (2022). We focus on the equilibrium M_{OBS}, $M_{\mathrm{OBS}} = E + W$, where E represents the entrainment rate at the sub-cloud layer top h, and W is the mesoscale vertical velocity. E is estimated using the classical flux-jump model (Lilly, 1968), adjusted to account for the finite-thickness transition layer at the sub-cloud layer top (Albright et al., 2022, 2023), as $E = \frac{A_{\mathrm{e}}\, \overline{w'\theta_{\mathrm{v}}'}\big|_{\mathrm{s}}}{\Delta\theta_{\mathrm{v}}}$. A_{e} is the effective entrainment efficiency, $\overline{w'\theta_{\mathrm{v}}'}\big|_{\mathrm{s}}$ is the surface buoyancy flux, and $\Delta\theta_{\mathrm{v}}$ is the θ_{v}-jump at the sub-cloud layer top (see Albright et al., 2022 and Vogel et al., 2022 for details). W is computed by vertically integrating the divergence of the horizontal wind field measured by the dropsondes (Bony & Stevens, 2019).

The robustness of W, E, the surface buoyancy flux, and the resulting M_{OBS} estimates was demonstrated with extensive sensitivity tests and independent data in Vogel et al. (2022), along with a detailed quantification of their corresponding uncertainties (see their Methods section for details). Note that using the equilibrium M_{OBS} and thus neglecting the temporal fluctuation and horizontal advection of h makes the estimates less noisy but does not influence the interpretation of the results in both the EUREC^{4}A data and large-eddy simulations (Vogel et al., 2020, 2022).

3.3. Diagnosing the Closure Parameters From EUREC^{4}A Observations

We use the EUREC^{4}A observations to diagnose all the parameters of the two closures. For the G01 closure, all parameters to compute w_* are determined from the HALO dropsonde data set (George et al., 2021), except for the SSTs used to compute the surface buoyancy flux. The sub-cloud layer top h is computed as the height where θ_{v} first exceeds its density-weighted mean from 100 m up to h by a fixed threshold of 0.2 K (see also Albright et al., 2022; Touzé-Peiffer et al., 2022). The threshold of 0.2 K represents about half of the average $\Delta\theta_{\mathrm{v}}$ of 0.36 K used for estimating E (Albright et al., 2022). The surface buoyancy flux is calculated with the Coupled Ocean-Atmosphere Response Experiment bulk flux algorithm version 3.6 (Edson et al., 2013; Fairall et al., 2003), using 20 m humidity, temperature, and wind data from the dropsondes, and SSTs extrapolated from R/V *Meteor* to the dropsonde position using a fixed zonal and meridional SST gradient of −0.14 K per degree derived from satellite SST data (see Vogel et al. (2022) for details).

For the PB09 closure, the TKE is computed from the velocity variances available in the ATR turbulence data (Brilouet et al., 2021). The TKE is averaged across the sub-cloud layer using all the 60 km long L-legs (i.e., the cloud-base rectangles and surface legs are excluded from the TKE here). We use both the vertical and horizontal contributions to the total TKE, that is $\mathrm{TKE} = \mathrm{TKE}_{\mathrm{hor}} + \mathrm{TKE}_{\mathrm{vert}} = \frac{1}{2}\left(\overline{(u')^2} + \overline{(v')^2} + \overline{(w')^2}\right)$, where the horizontal components refer to the zonal and meridional components of the wind. Note that turbulence data for the early flights (flights 4–8 from 26 to 31 January) were initially considered of poor quality (see Figure 14 of Brilouet et al., 2021), but later re-evaluated and deemed to have no obvious quality reductions.

CIN is computed from the HALO dropsonde data. Following Fletcher and Bretherton (2010), who developed a modified version of the PB09 closure, CIN is calculated as the vertically integrated negative buoyancy of a parcel with thermodynamic properties averaged between 200 and 400 m, lifted adiabatically from 300 m up to cloud base. Their cloud base is defined as the lifting condensation level of a parcel with a potential temperature θ corresponding to the mean θ between 200 and 400 m, and a specific humidity q_{v} corresponding to the mean plus standard deviation of q_{v} between 200 and 400 m (i.e., $\overline{q_{\mathrm{v}}} + \sigma_{q_{\mathrm{v}}}$), with $\sigma_{q_{\mathrm{v}}}$ computed here as the standard deviation

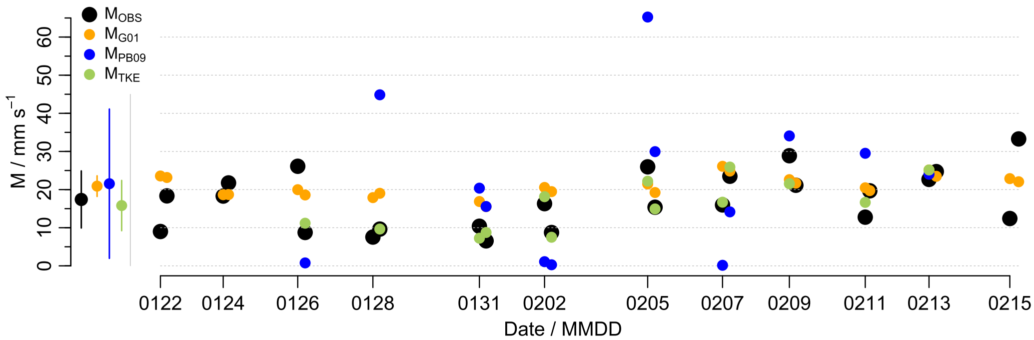

Figure 2. Timeseries of the observed mass flux M_{OBS}, the closures M_{G01} and M_{PB09}, and the best-fit linear regression M_{TKE} during the EUREC^{4}A campaign. The campaign mean ± one standard deviation of the estimates is shown on the left. Note that M_{PB09} and M_{TKE} estimates are only available for a subset of the dates, when ATR turbulence data is available.

of q_v over the same height range among the up to 36 individual dropsondes pertaining to a 3-circle set (The negative buoyancy between cloud base and the level of free convection is not accounted for in the definition of Fletcher and Bretherton (2010)).

4. Results and Discussion

4.1. Skill of Closures in Reproducing the Observed Cloud-Base Mass Flux

Figure 2 shows the timeseries of the reference M_{OBS} and the mass flux derived from the closures M_{G01} and M_{PB09} across the 1-month EUREC^{4}A campaign. Without any tuning, the G01 closure using w_* captures the mean M_{OBS} very well. The slight overestimation of the mean by 20% compared to M_{OBS} (Table A1) is likely due to M_{G01} targeting the cloud-core updraft mass flux, whereas M_{OBS} represents the total mass flux and thus implicitly includes contributions from downdrafts (i.e., contributions from cloud segments with negative vertical velocities). Additional analyses in Appendix A using the ATR turbulence data at cloud base show that the updraft mass flux is on average 25% larger than the total mass flux, explaining the differences in the mean M to a large degree.

The standard deviation of M_{OBS}, however, is strongly underestimated in M_{G01} (Figure 2 and Table A1). The correlation coefficient (R) between M_{G01} and M_{OBS} for the full sample of HALO data is $R = 0.47$. When considering only the reduced sample with coincident ATR turbulence data, the correlation increases to $R = 0.71$ (see Table A1). This sample-dependent difference in correlation strength is a coincidence and may be explained by the entrainment rate E tending to dominate variability in M_{OBS} for the sample with coincident ATR data, whereas W tends to dominate M_{OBS} variability for the three-circle sets with only HALO data available (not shown). E and w_* share the surface buoyancy flux as underlying data (see Sections 2 and 3.3), with the latter being strongly correlated to both w_* ($R = 0.97$) and E ($R = 0.93$). These results show the dependence of the skill of a closure on the predominant environmental conditions, illustrating that correctly predicting the environmental conditions in a climate model may be as important as the details of the closure itself.

The closure of PB09 overestimates the mean M_{OBS} by about 35% and its standard deviation by 270% (Table A1). A large part of the overestimation of the magnitude of M_{OBS} can again be explained by PB09 targeting the cloud-core updraft mass flux and not the total mass flux as is the case for M_{OBS} (see Appendix A). The PB09 closure explains 19% of the variance in M_{OBS} ($R = 0.43$). Overall, the additional complexity of the PB09 closure with its CIN-based area fraction scale does not help to explain the mass flux variability during EUREC^{4}A and leads to a poorer skill compared to the much simpler G01 closure. Note that we also tested the slightly modified version of the PB09 closure by Fletcher and Bretherton (2010). We find their $M_{\mathrm{FB10}} = 0.06\, w_{\mathrm{TKE}} \exp(-\mathrm{CIN}/\mathrm{TKE})$, with $w_{\mathrm{TKE}} = 0.28\sqrt{\mathrm{TKE}} + 0.64$ m s^{-1}, to strongly underestimate the magnitude and variability of M_{OBS} (mean ± σ of 5.29 ± 4.69 mm s^{-1}, and a correlation with M_{OBS} of $R = 0.25$).

When we look at the individual contributions of the area fraction (i.e., $\exp(-\mathrm{CIN}/\mathrm{TKE})$) and vertical velocity scale (i.e., $\sqrt{\mathrm{TKE}}$), we find the correlation of the area fraction scale with M_{OBS} to be much weaker ($R = 0.21$) than the correlation of the vertical velocity scale ($R = 0.90$). Hence, a TKE-based vertical velocity scale alone explains

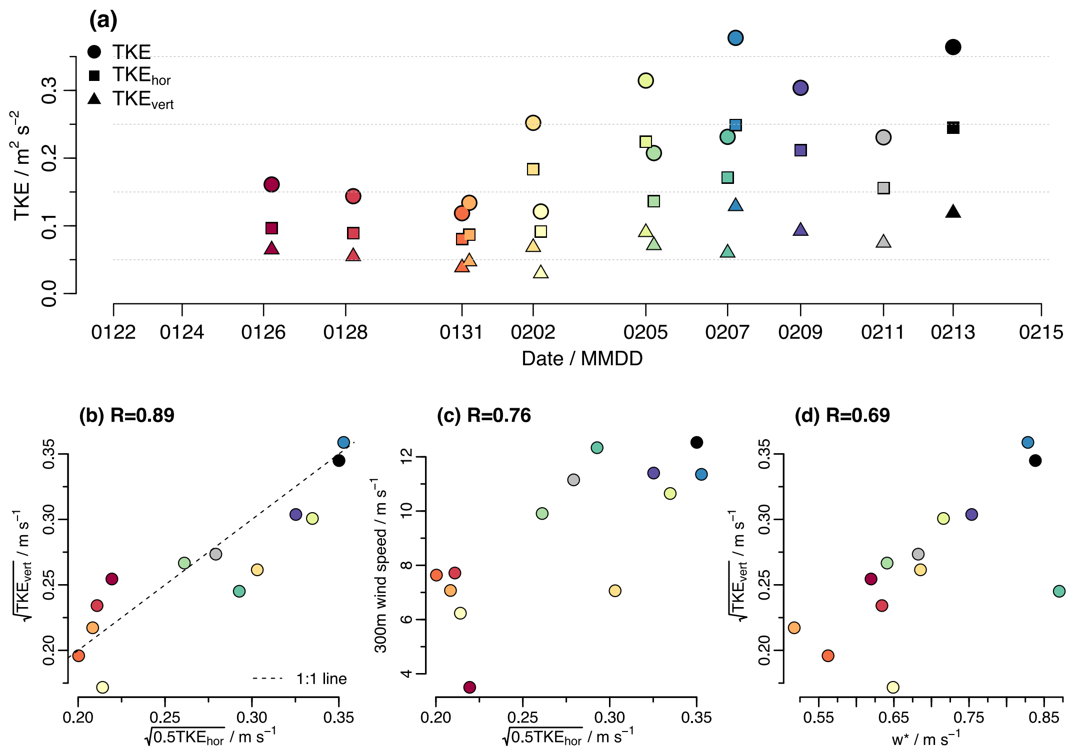

Figure 3. (a) Timeseries of the total turbulence kinetic energy and its horizontal and vertical contributions, TKE$_{hor}$ and TKE$_{vert}$, during the EUREC^{4}A campaign. (b–d) Relationships between (b) $\sqrt{0.5\text{TKE}_{hor}}$ and $\sqrt{\text{TKE}_{vert}}$, (c) $\sqrt{\text{TKE}_{hor}}$ and the mean wind speed at 300 m, and (d) w_* and $\sqrt{\text{TKE}_{vert}}$. The panel titles in (b–d) show the correlation coefficients of the two quantities. Panel (b) also shows the 1:1 line, and the different colors help distinguish the specific three-circle sets.

more than 80% of variance in M_{OBS} and outperforms the use of w_* in G01. We therefore also show the best-fit linear regression,

$$M_{\text{TKE}} = -0.017 + 0.069\sqrt{\text{TKE}}, \tag{4}$$

in Figure 2. The ability of the TKE to explain the cloud-base updraft velocity is consistent with mid-latitude continental Doppler lidar data (Zheng et al., 2021). That a TKE-based vertical velocity scale alone explains 80% of M_{OBS} variance is nevertheless surprising, as previous analyses of Doppler radar data at the Barbados Cloud Observatory (BCO) show the cloud fraction to dominate mass flux variability in non-raining trade cumuli (Klingebiel et al., 2021; Lamer et al., 2015). The next subsections address these points in more detail.

4.2. What Controls Variability in TKE?

Figure 3a shows a timeseries of the total TKE and the contributions of its horizontal and vertical components. We find the TKE to increase in the second half of the campaign, consistent with the increase in M_{OBS}. While Zheng et al. (2021) only consider the vertical component of TKE in their analyses, we find the horizontal components of the TKE to dominate the magnitude of the total TKE. The horizontal TKE has two components, $\overline{(u')^2}$ and $\overline{(v')^2}$, whose contributions are almost equal for our data (not shown).

In isotropic conditions, the horizontal TKE components together would be twice as large as the vertical component. To investigate the isotropy of the TKE during EUREC^{4}A, Figure 3b shows the relationship between $\sqrt{0.5\text{TKE}_{hor}}$ and $\sqrt{\text{TKE}_{vert}}$, which should fall on the 1:1 line if the TKE is isotropic. The TKE$_{hor}$ and TKE$_{vert}$ are overall very well correlated ($R = 0.89$), which is consistent with the steady winds in the measurement area. The horizontal wind at 300 m-height is on average 9 m s^{-1} and explains 58% of the variability in the horizontal TKE component (Figure 3c). Interestingly, the vertical TKE component tends to dominate at low TKE, while the horizontal components dominate at large TKE, leading to a certain S-shape of the relationship in Figure 3b. This observation is consistent with low TKE conditions being representative of more convective conditions, with weaker wind (see also Figure 3c) and TKE being generated in the vertical direction by buoyancy production. Contrastingly, large TKE conditions are more representative of shear-driven turbulence, with larger values of wind and TKE being generated in the horizontal direction by the shear production.

w_* represents the convective contribution to TKE through the surface buoyancy flux. Figure 3d shows that, apart from two outliers, w_* is very well correlated to the vertical component of TKE. The correlation of w_* and the total TKE is even larger ($R = 0.81$ instead of $R = 0.69$). Also wind shear can be important for TKE production, especially for the horizontal component and close to the surface (related to the friction velocity u_*) and the mixed-layer top (related to the shear between the sub-cloud and cloud layers). Whether convection or shear-driven turbulence dominates can be quantified with the stability parameter h/L_{OB}, where $L_{\mathrm{OB}} = \frac{-\overline{\theta_v}\, u_*^3}{k\, g \left(\overline{w'\theta_v'}\right)\big|_s}$ is the Obukhov length, with u_* computed from the vertical kinematic momentum fluxes at 60 m flight altitude, and k the von Kármán constant (set to 0.4). The resulting stability parameters are systematically smaller than -3.5, with a median of -10.7 (not shown). This indicates convection to dominate over shear (Wyngaard, 2010), suggesting that w_* should constrain the bulk statistics well. Nevertheless, the observation that the total TKE explains 30% more variability of M_{OBS} than w_* ($R = 0.90$ compared to $R = 0.71$) suggests that to get the cloud-base mass flux right needs information beyond bulk statistics.

Due to the strong correlation between the horizontal and vertical TKE components, however, it is not straightforward to attribute one-to-one the vertical TKE with the convective part and the horizontal TKE with the shear-driven part of the TKE. If there is more wind, there is more TKE in the horizontal through shear production. At the same time, more wind leads to larger surface fluxes, which lead to the correlation between TKE and w_* for large TKE (but not necessarily a causation, as the TKE is coming from the horizontal shear and not the convective forcing). A second complication is due to transfer terms related to the pressure-strain correlation, which are responsible for transfer of TKE between the vertical and horizontal components. These transfer terms can be derived from direct numerical simulations, showing that the transfer at the top of the sub-cloud layer can change sign depending on the relative importance between shear and convection (Fodor et al., 2022). Unfortunately, the transfer terms cannot be derived from our turbulence measurements.

4.3. Relative Importance of Vertical Velocity and Area Fraction Scales in Explaining Mass Flux Variability

As the TKE-based vertical velocity scale alone explains 80% of the variance in M_{OBS} during EUREC^{4}A, an additional area fraction scale does not seem to be necessary to accurately model the cloud-base mass flux. How can this finding be reconciled with vertically-pointing Doppler radar data from the BCO (Klingebiel et al., 2021; Lamer et al., 2015), which show cloud fraction to dominate mass flux variability in non-precipitating trade cumuli?

One reason could be that the TKE might implicitly contain information about the area fraction of sub-cloud layer thermals, which compose the roots of the clouds at the lifting condensation level. The TKE variability might thus not only represent the variability associated with the vertical velocity scale but also with the area fraction scale. A potential mechanism explaining how larger TKE leads to larger cloud fractions is that larger TKE leads to a deeper sub-cloud layer, which is associated with larger cloud bases. Such a mechanism is supported by the geometry of convective cells, as thermals at the root of the clouds usually scale with the sub-cloud layer depth h (Schmidt & Schumann, 1989; Schumann & Moeng, 1991). The data used here confirms a moderate correlation between TKE and h ($R = 0.71$). Larger cells therefore tend to be associated with larger velocities (represented through h in w_*, see Section 2), and they tend to be wider (Grabowski, 2023; Mulholland et al., 2021). However, these relationships might depend on the relative importance of shear versus convection and surface fluxes of moisture versus heat (Nuijens & Stevens, 2012), and on the role of gravity waves in shaping updraft size (Clark et al., 1986). More in-depth studies of the relation between sub-cloud layer thermals, TKE, and cloud fraction are needed to support these speculations.

Another reason why previous BCO analyses showed that cloud fraction dominates mass flux variability in the trade cumulus regime could be the neglect of mass flux contributions from precipitating trade cumuli, which presumably neglects the strongest up and downdraft mass fluxes. Rain drops have significant fall velocities and negatively bias the mean Doppler velocity, such that raining clouds were neglected in the previous studies (Klingebiel et al., 2021; Lamer et al., 2015). New techniques using the full Doppler velocity spectrum at high temporal frequency allow to retrieve the vertical air motion inside drizzling clouds (Zhu et al., 2021), which could help extend radar-based mass flux analyses to precipitating clouds. Lastly, the 13 mesoscale data points of coincident HALO and ATR data (representing a scale of 200 km and 3 hr) collected during nine days spread over half a month did not sample as much variability as the BCO data. The robustness of the results should thus be assessed in longer data sets, like the multi-year Doppler lidar and radar data at the BCO (Stevens et al., 2016).

5. Conclusion

Here we use observations from the recent EUREC^{4}A field campaign (Stevens et al., 2021) to evaluate the physical ideas behind two common closures for the shallow-convective mass flux at cloud base, M. We find that—without any tuning—both closures reproduce the magnitude of the observed mass flux M_{OBS} well and explain about 20% of its variability. What makes the two closures skillful is that they are based on solid physical ideas, with very general formulations that do not simply represent a best fit to a specific data set (see Equations 2 and 3). Nevertheless, the simple closure from Grant (2001) using only the surface-based convective velocity scale w_* underestimates the standard deviation of M_{OBS} about 2.8 times, and the more complicated closure of Park and Bretherton (2009) using a CIN-based area fraction scale and TKE-based vertical velocity scale overestimates it by 2.7 times. Interestingly, the additional complexity of the Park and Bretherton (2009) closure does not seem necessary to explain the mass flux during EUREC^{4}A, as the very simple Grant (2001) closure tends to perform better. This is in line with Neggers et al. (2004) whose evaluation of different mass flux closures with LES also showed the Grant (2001) closure to perform best.

We further find that a TKE-based vertical velocity scale alone explains 80% of M_{OBS} variability. This is surprising given previous Doppler radar analyses showing the cloud fraction to dominate mass flux variability at the BCO (Klingebiel et al., 2021; Lamer et al., 2015), but suggests that the TKE might implicitly contain information about the area fraction of thermals. Only representing the convective contribution to TKE through w_*, however, is not enough to represent the mass flux variability during EUREC^{4}A. The total TKE including both its horizontal and vertical components needs to be considered, as the strong trade winds make both the convective and shear-driven TKE contributions important.

This study would have benefited from a larger data set. The correlation of the Grant (2001) closure with the reference mass flux shows an explainable dependency on the sample size, with a higher correlation for the smaller sample with coincident ATR turbulence data compared to the larger sample with only HALO dropsonde data. It will thus be important to revisit these results with more data, for example from the extensive turbulence measurements at the BCO (Stevens et al., 2016) or with more realistic large-eddy simulations with open boundary conditions (e.g., Schulz & Stevens, 2023).

Overall, our study highlights that the accuracy and scale of recent observations like the EUREC^{4}A data are suitable for answering questions about microscale-mesoscale interactions—in this case, questions about the physical assumptions in mass flux closures for shallow convection. The strong connection between the TKE and mass flux provides a pathway to better represent shallow convection in km-scale models by accounting for its tight coupling to the sub-cloud layer turbulence.

Appendix A: Cloud-Core Updraft Mass Flux Versus Total Mass Flux

The ATR turbulence data can also be used to calculate the mass flux directly as the product of the cloud fraction and the in-cloud vertical velocity along the rectangular cloud-base flight track (see also Vogel et al., 2022). The cloud fraction is computed from the high-frequency (25 Hz) humidity sensor, where relative humidity $\geq$98% is defined as cloudy. The in-cloud vertical velocity is the vertical velocity averaged over the cloudy areas. The data also allows to distinguish between the total mass flux of all cloudy areas (denoted as M_{ATR}, including the downdraft portions of clouds) and a cloud-core updraft mass flux that only includes those portions of the clouds having positive vertical velocity ($M_{\mathrm{up,ATR}}$).

Table A1 shows that the cloud-core updraft mass flux $M_{\mathrm{up,\ ATR}}$ is about 25% larger than the total mass flux M_{ATR}. The difference between core and total mass flux can therefore explain to a large degree the overestimation of the

Table A1
Mean and Standard Deviation of the Mass Flux Estimates ($\overline{M}$ and σ_M), as Well as the Correlation Coefficient R Between the Respective Mass Fluxes and the Reference M_{OBS}

	$\overline{M}$			σ_M			R		
	All	ATR	ATR cb	All	ATR	ATR cb	All	ATR	ATR cb
M_{OBS}	17.41	15.81	15.06	7.49	7.32	7.60	1.00	1.00	1.00
M_{G01}	20.90	20.76	20.41	2.71	3.20	3.24	0.47	0.71	0.67
M_{PB09}	–	21.54	24.07	–	19.58	20.15	–	0.43	0.54
M_{TKE}	–	15.81	14.68	–	6.59	6.33	–	0.90	0.90
M_{ATR}	–	–	12.62	–	-	8.21	–	–	0.78
$M_{\mathrm{up,ATR}}$	–	–	15.77	–	-	9.46	–	–	0.76

Note. The values are given for the full sample of HALO 3-circle sets ("all"), the reduced sample with coincident ATR data ("ATR"), and the smaller sample of consistent ATR cloud-base data ("ATR cb"). $\overline{M}$ and σ_M are in units of mm s^{-1}.

mean mass flux of the two closures discussed in Section 4.1, as the closures target the core and not the total mass flux. M_{ATR} and $M_{\mathrm{up,ATR}}$ happen to be perfectly correlated ($R = 1$), lending confidence in the comparison of variability between M_{OBS} and the closures M_{G01} and M_{PB09} in this paper. Both the cloud fraction ($R = 0.94$) and in-cloud vertical velocity ($R = 0.88$) are strongly correlated to M_{ATR}.

Note that the data sample for which the cloud-base M_{ATR} and $M_{\mathrm{up,ATR}}$ can be compared to the other estimates (referred to as "ATR cb" in Table A1) is smaller than the sample for which ATR sub-cloud layer turbulence measurements are available (sample "ATR"), because two three-circle sets are excluded due to inconsistent sampling of mesoscale variability between the HALO and ATR aircraft (for details see Vogel et al., 2022). Table A1 shows that the two ATR data samples yield very similar statistics for the best-fit M_{TKE} and the two closures (except for the correlation of M_{PB09} and M_{OBS} improving to $R = 0.54$), so the conclusions of our study are not affected by these differences in data samples.

It is somewhat surprising that the direct mass flux measurements from ATR at cloud base, M_{ATR} and $M_{\mathrm{up,ATR}}$, are less well correlated to the reference M_{OBS} than the TKE-based best fit estimate M_{TKE}. The cloud sampling along the cloud-base rectangles seems therefore less statistically representative than the sampling of turbulent eddies along the sub-cloud layer legs, which were also flown more in the center of the EUREC^{4}A circle compared to the cloud base rectangles in the western portion of the circle (see Figure 1).

Acknowledgments
The authors thank Pierre-Etienne Brilouet and Marie Lothon for creating the ATR turbulence data set and making it so easy to use, Sandrine Bony for creating the ATR cloud-base mass fluxes, and Bjorn Stevens for creating Figure 1. We acknowledge helpful discussions with Nicolas Rochetin, Sandrine Bony, Nicolas Maury, Marie Lothon, and Fleur Couvreux. We also acknowledge the efforts of the entire EUREC^{4}A team for collecting and processing the EUREC^{4}A data. We thank Margaret LeMone for her insightful review. Raphaela Vogel acknowledges support from the ERC starting grant ROTOR (Grant 101116282) and the Deutsche Forschungsgemeinschaft (DFG, German Research Foundation) under Germany's Excellence Strategy—EXC 2037 'CLICCS - Climate, Climatic Change, and Society'—Project Number: 390683824, contribution to the Center for Earth System Research and Sustainability (CEN) of Universität Hamburg. We further acknowledge financial support from the Open Access Publication Fund of Universität Hamburg. Open Access funding enabled and organized by Projekt DEAL.

Data Availability Statement

All data used in this study are openly available and published in the EUREC^{4}A database of AERIS (https://eurec4a.aeris-data.fr/, last accessed: 28 November 2023). Specifically, we use v2.0.0 of the JOANNE dropsonde data (https://doi.org/10.25326/246, see George et al. (2021) for details) and v2.0 of the ATR turbulence measurements (https://doi.org/10.25326/128, see Brilouet et al. (2021) for details). See also Vogel et al. (2022) for further details on the data used for computing the surface buoyancy flux and for estimating and evaluating the reference observed mass flux. General information on the aircraft operations can be found in the respective overview papers of the HALO (Konow et al., 2021) and ATR aircraft (Bony et al., 2022).

References

Albright, A. L., Bony, S., Stevens, B., & Vogel, R. (2022). Observed subcloud-layer moisture and heat budgets in the trades. *Journal of the Atmospheric Sciences*, *79*(9), 2363–2385. https://doi.org/10.1175/JAS-D-21-0337.1

Albright, A. L., Stevens, B., Bony, S., & Vogel, R. (2023). A new conceptual picture of the trade wind transition layer. *Journal of the Atmospheric Sciences*, *80*(6), 1547–1563. https://doi.org/10.1175/JAS-D-22-0184.1

Arakawa, A., & Schubert, W. H. (1974). Interaction of a cumulus cloud ensemble with the large-scale environment, part i. *Journal of the Atmospheric Sciences*, *31*(3), 674–701. https://doi.org/10.1175/1520-0469(1974)031⟨0674:IOACCE⟩2.0.CO;2

Augstein, E., Riehl, H., Ostapoff, F., & Wagner, V. (1973). Mass and energy transports in an undisturbed Atlantic trade-wind flow. *Monthly Weather Review*, *101*(2), 101–111. https://doi.org/10.1175/1520-0493(1973)101<0101:maetia>2.3.co;2

Becker, T., Bechtold, P., & Sandu, I. (2021). Characteristics of convective precipitation over tropical Africa in storm-resolving global simulations. *Quart. J. Roy. Meteor. Soc.*, *147*(741), 4388–4407. https://doi.org/10.1002/qj.4185

Bony, S., Lothon, M., Delanoë, J., Coutris, P., Etienne, J.-C., Aemisegger, F., et al. (2022). EUREC^{4}A observations from the SAFIRE ATR42 aircraft. *Earth System Science Data*, *14*(4), 2021–2064. https://doi.org/10.5194/essd-14-2021-2022

Bony, S., & Stevens, B. (2019). Measuring area-averaged vertical motions with dropsondes. *Journal of the Atmospheric Sciences*, *76*(3), 767–783. https://doi.org/10.1175/JAS-D-18-0141.1

Bony, S., Stevens, B., Ament, F., Bigorre, S., Chazette, P., Crewell, S., et al. (2017). EUREC^{4}A: A field campaign to elucidate the couplings between clouds, convection and circulation. *Surveys in Geophysics*, *38*(6), 1529–1568. https://doi.org/10.1007/s10712-017-9428-0

Bretherton, C. S., McCaa, J. R., & Grenier, H. (2004). A new parameterization for shallow cumulus convection and its application to marine subtropical cloud-topped boundary layers. Part I: Description and 1d results. *Monthly Weather Review*, *132*(4), 864–882. https://doi.org/10.1175/1520-0493(2004)132⟨0864:ANPFSC⟩2.0.CO;2

Brilouet, P.-E., Lothon, M., Etienne, J.-C., Richard, P., Bony, S., Lernoult, J., et al. (2021). The EUREC^{4}A turbulence dataset derived from the safire atr 42 aircraft. *Earth System Science Data*, *13*(7), 3379–3398. https://doi.org/10.5194/essd-13-3379-2021

Clark, T. L., Hauf, T., & Kuettner, J. P. (1986). Convectively forced internal gravity waves: Results from two-dimensional numerical experiments. *Quart. J. Roy. Meteor. Soc.*, *112*(474), 899–925. https://doi.org/10.1002/qj.49711247402

Deardorff, J. W. (1970). Convective velocity and temperature scales for the unstable planetary boundary layer and for Rayleigh convection. *Journal of the Atmospheric Sciences*, *27*(8), 1211–1213. https://doi.org/10.1175/1520-0469(1970)027⟨1211:CVATSF⟩2.0.CO;2

de Rooy, W. C., Siebesma, P., Baas, P., Lenderink, G., de Roode, S. R., de Vries, H., et al. (2022). Model development in practice: A comprehensive update to the boundary layer schemes in harmonie-arome cycle 40. *Geoscientific Model Development*, *15*(4), 1513–1543. https://doi.org/10.5194/gmd-15-1513-2022

Edson, J. B., Jampana, V., Weller, R. A., Bigorre, S. P., Plueddemann, A. J., Fairall, C. W., et al. (2013). On the exchange of momentum over the open ocean. *Journal of Physical Oceanography*, *43*(8), 1589–1610. https://doi.org/10.1175/JPO-D-12-0173.1

Esbensen, S. (1975). An analysis of subeloud-layer heat and moisture budgets in the western atlantic trades. *Journal of the Atmospheric Sciences*, *32*(10), 1921–1933. https://doi.org/10.1175/1520-0469(1975)032⟨1921:AAOSLH⟩2.0.CO;2

Fairall, C. W., Bradley, E. F., Hare, J. E., Grachev, A. A., & Edson, J. B. (2003). Bulk parameterization of air-sea fluxes: Updates and verification for the coare algorithm. *Journal of Climate*, *16*(4), 571–591. https://doi.org/10.1175/1520-0442(2003)016⟨0571:BPOASF⟩2.0.CO;2

Fletcher, J. K., & Bretherton, C. S. (2010). Evaluating boundary LayerBased mass flux closures using cloud-resolving model simulations of deep convection. *Journal of the Atmospheric Sciences*, *67*(7), 2212–2225. https://doi.org/10.1175/2010JAS3328.1

Fodor, K., Mellado, J. P., & Haghshenas, A. (2022). On the non-monotonic variation of the entrainment buoyancy flux with wind shear. *Boundary-Layer Meteorology*, *184*(3), 463–477. https://doi.org/10.1007/s10546-022-00712-x

George, G., Stevens, B., Bony, S., Pincus, R., Fairall, C., Schulz, H., et al. (2021). Joanne: Joint dropsonde observations of the atmosphere in tropical north Atlantic meso-scale environments. *Earth System Science Data*, *13*(11), 5253–5272. https://doi.org/10.5194/essd-13-5253-2021

Grabowski, W. W. (2023). Daytime convective development over land: The role of surface forcing. *Quart. J. Roy. Meteor. Soc.*, *149*(756), 2800–2819. https://doi.org/10.1002/qj.4532

Grant, A. L. M. (2001). Cloud-base fluxes in the cumulus-capped boundary layer. *Quart. J. Roy. Meteor. Soc.*, *127*(572), 407–421. https://doi.org/10.1002/qj.49712757209

Klingebiel, M., Konow, H., & Stevens, B. (2021). Measuring shallow convective mass flux profiles in the trade wind region. *Journal of the Atmospheric Sciences*, *78*(10), 3205–3214. https://doi.org/10.1175/JAS-D-20-0347.1

Konow, H., Ewald, F., George, G., Jacob, M., Klingebiel, M., Kölling, T., et al. (2021). EUREC^{4}A'S *HALO*. *Earth System Science Data*, *13*(12), 5545–5563. https://doi.org/10.5194/essd-13-5545-2021

Lamer, K., Kollias, P., & Nuijens, L. (2015). Observations of the variability of shallow trade wind cumulus cloudiness and mass flux. *Journal of Geophysical Research: Atmospheres*, *120*(12), 6161–6178. https://doi.org/10.1002/2014JD022950

LeMone, M. A., & Pennell, W. T. (1976). The relationship of trade wind cumulus distribution to subcloud layer fluxes and structure. *Monthly Weather Review*, *104*(5), 524–539. https://doi.org/10.1175/1520-0493(1976)104⟨0524:TROTWC⟩2.0.CO;2

Lilly, D. K. (1968). Models of cloud-topped mixed layers under a strong inversion. *Quart. J. Roy. Meteor. Soc.*, *94*(401), 292–309. https://doi.org/10.1002/qj.49709440106

Mulholland, J. P., Peters, J. M., & Morrison, H. (2021). How does lcl height influence deep convective updraft width? *Geophysical Research Letters*, *48*(13), e2021GL093316. https://doi.org/10.1029/2021GL093316

Neggers, R. A. J. (2015). Exploring bin-macrophysics models for moist convective transport and clouds. *Journal of Advances in Modeling Earth Systems*, *7*(4), 2079–2104. https://doi.org/10.1002/2015ms000502

Neggers, R. A. J., Köhler, M., & Beljaars, A. C. M. (2009). A dual mass flux framework for boundary layer convection. Part I: Transport. *Journal of the Atmospheric Sciences*, *66*(6), 1465–1487. https://doi.org/10.1175/2008JAS2635.1

Neggers, R. A. J., Siebesma, A. P., Lenderink, G., & Holtslag, A. A. M. (2004). An evaluation of mass flux closures for diurnal cycles of shallow cumulus. *Monthly Weather Review*, *132*(11), 2525–2538. https://doi.org/10.1175/MWR2776.1

Nicholls, S., & LeMone, M. (1980). The fair weather boundary layer in gate: The relationship of subcloud fluxes and structure to the distribution and enhancement of cumulus clouds. *Journal of the Atmospheric Sciences*, *37*(9), 2051–2067. https://doi.org/10.1175/1520-0469(1980)037<2051:tfwbli>2.0.co;2

Nuijens, L., & Stevens, B. (2012). The influence of wind speed on shallow marine cumulus convection. *Journal of the Atmospheric Sciences*, *69*(1), 168–184. https://doi.org/10.1175/JAS-D-11-02.1

Park, S., & Bretherton, C. S. (2009). The university of Washington shallow convection and moist turbulence schemes and their impact on climate simulations with the community atmosphere model. *Journal of Climate*, *22*(12), 3449–3469. https://doi.org/10.1175/2008JCLI2557.1

Schmidt, H., & Schumann, U. (1989). Coherent structure of the convective boundary layer derived from large-eddy simulations. *Journal of Fluid Mechanics*, *200*, 511–562. https://doi.org/10.1017/s0022112089000753

Schulz, H., & Stevens, B. (2023). Evaluating large-domain, hecto-meter, large-eddy simulations of trade-wind clouds using eurec4a data. *Journal of Advances in Modeling Earth Systems*, *15*(10), e2023MS003648. https://doi.org/10.1029/2023MS003648

Schumann, U., & Moeng, C.-H. (1991). Plume fluxes in clear and cloudy convective boundary layers. *Journal of the Atmospheric Sciences*, *48*(15), 1746–1757. https://doi.org/10.1175/1520-0469(1991)048⟨1746:PFICAC⟩2.0.CO;2

Sherwood, S. C., Bony, S., & Dufresne, J.-L. (2014). Spread in model climate sensitivity traced to atmospheric convective mixing. *Nature*, *505*(7481), 37–42. https://doi.org/10.1038/nature12829

Siebesma, A. P., Bony, S., Jakob, C., & Stevens, B. (Eds.) (2020)., *Clouds and climate: Climate science's greatest challenge*. Cambridge University Press. https://doi.org/10.1017/9781107447738

Siebesma, A. P., Soares, P. M. M., & Teixeira, J. (2007). A combined eddy-diffusivity mass-flux approach for the convective boundary layer. *Journal of the Atmospheric Sciences*, *64*(4), 1230–1248. https://doi.org/10.1175/JAS3888.1

Soares, P., Miranda, P., Siebesma, A., & Teixeira, J. (2004). An eddy-diffusivity/mass-flux parametrization for dry and shallow cumulus convection. *Quarterly Journal of the Royal Meteorological Society*, *130*(604), 3365–3383. https://doi.org/10.1256/qj.03.223

Stevens, B., Bony, S., Farrell, D., Ament, F., Blyth, A., Fairall, C., et al. (2021). EUREC^{4}A. *Earth System Science Data*, *13*(8), 4067–4119. https://doi.org/10.5194/essd-13-4067-2021

Stevens, B., Farrell, D., Hirsch, L., Jansen, F., Nuijens, L., Serikov, I., et al. (2016). The Barbados cloud observatory: Anchoring investigations of clouds and circulation on the edge of the ITCZ. *Bulletin America Meteorology Social*, *97*(5), 787–801. https://doi.org/10.1175/BAMS-D-14-00247.1

Stevens, B., Satoh, M., Auger, L., Biercamp, J., Bretherton, C. S., Chen, X., et al. (2019). Dyamond: The dynamics of the atmospheric general circulation modeled on non-hydrostatic domains. *Progress in Earth and Planetary Science*, *6*(1), 61. https://doi.org/10.1186/s40645-019-0304-z

Suselj, K., Kurowski, M. J., & Teixeira, J. (2019). A unified eddy-diffusivity/mass-flux approach for modeling atmospheric convection. *Journal of the Atmospheric Sciences*, *76*(8), 2505–2537. https://doi.org/10.1175/jas-d-18-0239.1

Tatebe, H., Ogura, T., Nitta, T., Komuro, Y., Ogochi, K., Takemura, T., et al. (2019). Description and basic evaluation of simulated mean state, internal variability, and climate sensitivity in MIROC6. Geosci. *Model Dev.*, *12*(7), 2727–2765. https://doi.org/10.5194/gmd-12-2727-2019

Touzé-Peiffer, L., Vogel, R., & Rochetin, N. (2022). Cold pools observed during EUREC4A: Detection and characterization from atmospheric soundings. *Journal of Applied Meteorology and Climatology*, *61*(5), 593–610. https://doi.org/10.1175/JAMC-D-21-0048.1

Vial, J., Albright, A. L., Vogel, R., Musat, I., & Bony, S. (2023). Cloud transition across the daily cycle illuminates model responses of trade cumuli to warming. *Proceedings of the National Academy of Sciences*, *120*(8), e2209805120. https://doi.org/10.1073/pnas.2209805120

Vial, J., Bony, S., Dufresne, J.-L., & Roehrig, R. (2016). Coupling between lower-tropospheric convective mixing and low-level clouds: Physical mechanisms and dependence on convection scheme. *Journal of Advances in Modeling Earth Systems*, *8*(4), 1892–1911. https://doi.org/10.1002/2016MS000740

Vogel, R., Albright, A. L., Vial, J., George, G., Stevens, B., & Bony, S. (2022). Strong cloud–circulation coupling explains weak trade cumulus feedback. *Nature*, *612*(7941), 696–700. https://doi.org/10.1038/s41586-022-05364-y

Vogel, R., Bony, S., & Stevens, B. (2020). Estimating the shallow convective mass flux from the subcloud-layer mass budget. *Journal of the Atmospheric Sciences*, *77*(5), 1559–1574. https://doi.org/10.1175/JAS-D-19-0135.1

Vogel, R., Konow, H., Schulz, H., & Zuidema, P. (2021). A climatology of trade-wind cumulus cold pools and their link to mesoscale cloud organization. *Atmospheric Chemistry and Physics*, *21*(21), 16609–16630. https://doi.org/10.5194/acp-21-16609-2021

von Salzen, K., Scinocca, J. F., McFarlane, N. A., Li, J., Cole, J. N. S., Plummer, D., et al. (2013). The Canadian fourth generation atmospheric global climate model (CanAM4). Part I: Representation of physical processes. *Atmosphere-Ocean*, *51*(1), 104–125. https://doi.org/10.1080/07055900.2012.755610

Walters, D., Boutle, I., Brooks, M., Melvin, T., Stratton, R., Vosper, S., et al. (2017). The met office unified model global atmosphere 6.0/6.1 and jules global land 6.0/6.1 configurations. *Geoscientific Model Development*, *10*(4), 1487–1520. https://doi.org/10.5194/gmd-10-1487-2017

Witte, M. K., Herrington, A., Teixeira, J., Kurowski, M. J., Chinita, M. J., Storer, R. L., et al. (2022). Augmenting the double-Gaussian representation of atmospheric turbulence and convection via a coupled stochastic multi-plume mass-flux scheme. *Monthly Weather Review*, *150*(9), 2339–2355. https://doi.org/10.1175/mwr-d-21-0215.1

Wyngaard, J. C. (2010). *Turbulence in the atmosphere*. Cambridge University Press.

Zheng, Y., Rosenfeld, D., & Li, Z. (2021). Sub-cloud turbulence explains cloud-base updrafts for shallow cumulus ensembles: First observational evidence. *Geophysical Research Letters*, *48*(6), e2020GL091881. https://doi.org/10.1029/2020GL091881

Zhu, Z., Kollias, P., Yang, F., & Luke, E. (2021). On the estimation of in-cloud vertical air motion using radar Doppler spectra. *Geophysical Research Letters*, *48*(1), e2020GL090682. https://doi.org/10.1029/2020GL090682